Chapter 5 : NTCL-Based Temperature Sensing and LFP Visualization Using $CaMoO_4$: $Ho^{3+}/Tm^{3+}/Yb^{3+}$ Phosphors

5.1 Introduction

In chapter 3 and chapter 4 we have explained in detail the structural, optical properties and thermally coupled level-based temperature sensing in Er^{3+}/Yb^{3+} co-doped $CaMoO_4$ phosphor. We have also discussed the effect of size and Bi^{3+} co-doping in Er^{3+}/Yb^{3+}; $CaMoO_4$. Now here in this chapter we have used Ho^{3+} and Tm^{3+} for dual luminescent centres. The different emission band of these two lanthanides has been used for non-thermally coupled levels-based temperature sensing application. The detailed theory of these two techniques for temperature sensing has been demonstrated in detail in chapter 1. We have also used $CaMoO_4$: $Ho^{3+}/Tm^{3+}/Yb^{3+}$ phosphor for latent fingerprinting application in this chapter.

Temperature is the most fundamental physical parameter, and their precise measurement is crucial for scientific study, metallurgy, electronics, industries, biological sciences, and other fields. Researchers mostly emphasize the fluorescence intensity ratio (FIR) methodology, recorded as a function of temperature, owing to its straightforward implementation and ability to provide accurate precision. Generally, the FIR involves the measurement of emission intensity commencing from two thermally coupled levels (TCLs) governed by Maxell's Boltzmann distribution law. Nevertheless, this approach has significant challenges, including prolonged response time, limited sensitivity, thermal lag, non-linearity constraints, and in certain instances, inadequate spatial resolution [147]. The emission acquisition from two non-thermally coupled levels (NTCLs) associated with either a single or two different Ln^{3+} ions have significant temperature sensitivity, which opens one of the emerging alternatives.

One of the expanding uses of Ln^{3+} activated phosphor materials is the development of multi-coloured latent fingerprints (LFPs) using the phosphor materials. Latent fingerprinting is a vital tool in forensic investigation, facilitating the identification of individuals by developing distinctive ridge patterns left over different surfaces. Conventional techniques for developing latent fingerprints frequently rely on powders or chemical reagents, that can be constrained by ambient conditions and substrate compatibility. Recent improvements in Ln^{3+}-activated phosphor materials have opened new avenues for enhancing the visibility and endurance of latent fingerprints, providing a more reliable and effective method to improve the contrast of latent prints against diverse backgrounds and different colour visualization [148].

This study presents highly sensitive FIR thermometry employing NTCLs of $CaMoO_4:Ho^{3+}/Tm^{3+}/Yb^{3+}$ phosphors, which generates an intense glow of Ho^{3+} and Tm^{3+} ions as upconversion emission under NIR excitation. However, to the best of our knowledge, this host has not been tried for the NTCLs-based optical thermometry so far.

The selection of appropriate dopant ions, optimization of their concentration, and choice of a suitable synthesis route is the key to fetch intense, and reliable emission. As luminescent centres, the Ho^{3+} ion is recognized for its emissions in the green ($^5F_4$, $^5S_2 \rightarrow {}^5I_8$), red ($^5F_5 \rightarrow {}^5I_8$), and near-infrared ($^5F_4$, $^5S_2 \rightarrow {}^5I_7$) regions, with green and red emissions exhibiting significant intensity in selected host with low phonon frequency. Among these, the $^5F_4$ and $^5S_2$ levels are thermally coupled, as documented by multiple investigations for temperature sensing; nonetheless, the energy gap ($\Delta E \sim 250$ cm^{-1}) between the two levels exhibits limitations regarding spatial resolution [146]. On the other hand, the significant emission of Tm^{3+} ions are seen in the blue ($^1G_4 \rightarrow {}^3H_6$) and near-infrared ($^3H_4 \rightarrow {}^3H_6$) regions, as well as the temperature-dependent thermally coupled emission in the red region ($^3F_{2,3}$ and $^3H_4 \rightarrow {}^3H_6$).

Conversely, the Yb^{3+} ions ($^2F_{5/2} \rightarrow {}^2F_{7/2}$) serve as sensitizers by efficiently transferring energy to both Ho^{3+} and Tm^{3+} ions [149]. The hydrothermal synthesis route is a viable and cost-effective methodology that offers numerous advantages, including low reaction temperatures, shorter reaction times, and controlled particle size and morphology, which facilitate the scaling up of synthesized materials without requiring intermediate materials/procedures. These characteristics all together offer a perfect choice for synthesizing phosphor materials with tailored properties [150].

This chapter primarily aims to synthesize $CaMoO_4$ phosphor materials doped with Ho/Yb, Tm/Yb, and Ho/Tm/Yb using a hydrothermal approach at 180°C, followed by calcination at higher temperatures to improve structural and optical properties. The phase growth, morphology, and associated vibrational modes of the host have been meticulously examined using XRD, SEM, and FTIR techniques. At the same time, the optical absorption of the synthesized materials is assessed using UV-Vis absorption technique. The optical emission characteristics of the synthesized phosphor materials were investigated under NIR excitation (λ_{exci}=980 nm), accompanied by a comprehensive power-dependent upconversion luminescence analysis to evaluate the involvement of a number of photons for a particular UC transition. Phosphorus materials' temperature sensing properties are determined by evaluating temperature-dependent UC measurements between 300 – 572 K. Whereas "powder dusting approach" was employed to generate LPFs left on a glass slide, and a camera equipped with a particular filter was used to record the results under NIR illumination.

5.2 Synthesis procedure

All phosphor samples were synthesized using a facile hydrothermal treatment at 180°C post-calcinated at 750°C to remove undesired reactants with improved

crystallinity[151]. The starting AR grade precursors, $Ca(NO_3)_2.4H_2O$ (98%), $(NH_4)_6Mo_7O_{24}.4H_2O$ (99.0%). In contrast, the lanthanides dopants i.e., Ho_2O_3 (99.9%), Tm_2O_3 (99.99%) and Yb_2O_3 (99.99%) were obtained from Alfa Aesar. All the chemicals were used without any further post-treatment. Initially, the REs oxides were dissolved in a dilute nitric acid (Fisher Scientific) at 80°C to convert them into metal nitrates chemically. After this, these metal nitrates were washed 2-3 times in doubly deionized water to remove the nitric acid traces. Now, the 5 ml aqueous solution of REs nitrates in deionized water was prepared in beakers separately for further use.

As in a typical hydrothermal process, the water-soluble stochiometric amounts of precursors for different samples were dissolved in deionized water, preheated at 80°C and vigorously stirred for 2 h to get the uniform solution. Now, the whole solution was poured into an autoclave and kept at a temperature of 140 °C for hydrothermal treatment for 24 h. After cooling down the autoclave to room temperature, the samples were collected by centrifugation and washed 2-3 times using ethanol and water. A white powder sample is then obtained and placed for post-treatment at 750 °C for 3 h to improve crystallinity. A similar synthesis method is adopted for each sample.

5.3 Result and discussions

5.3.1 Phase, particle shape/size, and elemental mapping analysis

XRD (X-ray diffraction) measurements were carried out to determine the phase and crystalline structure of the phosphor samples sintered at 750°C. The optimized doubly and triply doped phosphor samples are designated as $CaMoO_4:Ho^{3+}/Yb^{3+}$ (CMOHY), $CaMoO_4:Tm^{3+}/Yb^{3+}$ (CMOTY), and $CaMoO_4:Ho^{3+}/Tm^{3+}/Yb^{3+}$ (CMOHTY) phosphors,

respectively, for their respective demonstrations. The XRD patterns of the pristine CMO, as well as the optimized samples CMOHY, CMOTY, and CMOHTY, reveal the formation of a scheelite-type tetragonal structure with I $4_1/a$ space group [JCPDS: 29-0351] and T_d symmetry [9]. Fig. 5.1(a) depicts the diffraction patterns of phosphor samples, which align with previously reported data, substantiating well formation of the calcium molybdate framework.[8] While the absence of impurity peaks signifies the successful incorporation of Ho^{3+} (1.015Å)/ Tm^{3+} (0.994 Å) /Yb^{3+} (0.985 Å) in the CMO lattice. Despite the disparity in valency between Ca^{2+} (1.12 Å) and doped Ln^{3+} ions, the proximity of ionic radii facilitates lattice doping and does not affect the lattice structure. The crystalline structure of $CaMoO_4$ consists of a tetrahedron of MoO_4 connected to a dodecahedron (CaO_8) at shared vertices, as seen in the Fig. 5.1(b).

The average crystallite sizes of the CMO, CMOHY, CMOTY, and CMOHTY samples are calculated using the Debye-Scherrer equation [152]:

$$D = \frac{0.89\lambda}{\beta cos\theta} \quad \dots (5.1)$$

Here, D represents the average crystallite size, λ (1.54 Å) denotes the wavelength of the used X-rays, and β signifies the full width at half maximum (FWHM) of diffraction peaks. The estimated average crystallite sizes for CMO, CMOHY, CMOTY, and CMOHTY are 54 nm, 58 nm, 64 nm, and 72 nm, respectively. Thus, the optimized lanthanide doping causes an enhancement in the crystallite size, which also owe to improved optical characteristics. Furthermore, the indirect approach for estimating dislocation density (δ):

$$\delta = 1/D^2 \quad \dots (5.2)$$

Here, D is the estimated crystallite size facilitates the initial evaluation of crystallographic defects or irregularities. The determined dislocation densities of CMO, CMOHY, CMOTY and CMOHTY are 34.29×10^{13} m^{-2}, 29.72×10^{13} m^{-2}, 24.41×10^{13} m^{-2}, and 19.29×10^{13} m^{-2}, respectively. The reducing dislocation densities with lanthanide doping signifies the reduction in defect and also would lead to enhanced optical properties [153].

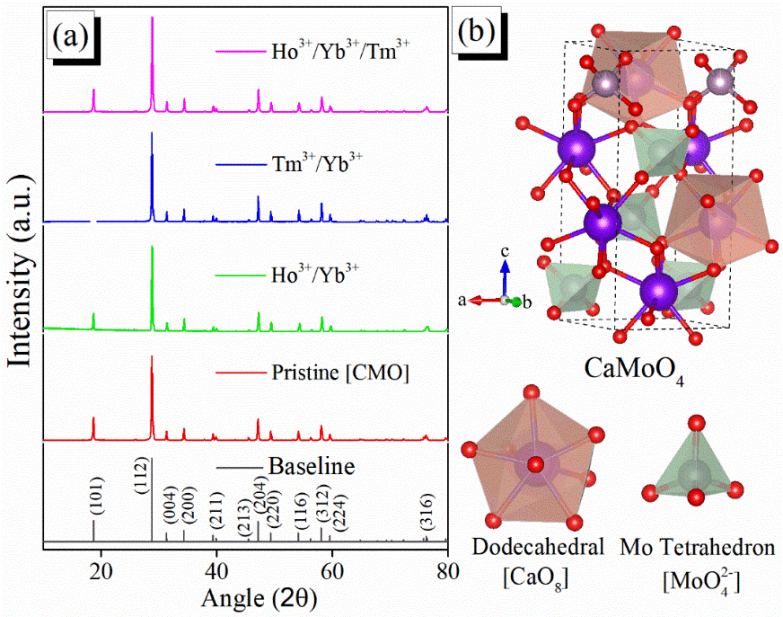

Figure 5.1 (a) X-ray diffraction patterns of pristine CMO, CMOHY, CMOTY, and CMOHTY phosphors materials sintered at 750°C, (b) Tetragonal crystalline lattice of $CaMoO_4$.

Moreover, Rietveld refinement of the developed phosphor samples has been accomplished using the 'Fullprof Suite' (5.10) program, employing the XRD data as initial parameters for evaluating the lattice parameters. The Pseudo-Voigt peak shape function was used to fit the diffraction peaks, while a linear interpolation function with refinable heights was employed as the background function. Fig. 5.2 depicts the refinement plots along with goodness of fitting, whilst Table 5.1 summarizes the structural parameters and residuals of the refinement. The structural refinement further corroborates the establishment of tetragonal phase with I 41/a space group, and denied the presence of impurities peaks. This similarity can be attributed to the comparable ionic radii of the dopant ions (Ho^{3+}, Tm^{3+}, and Yb^{3+}) with

the Ca^{2+} ion. As a result, it is possible to conclude that different Ln^{3+} were successfully incorporated into the pure $CaMoO_4$ sample [9].

Table 5.1 List of refined structural parameters and residuals of refinements of four different powder samples: CMO, CMOHY, CMOTY, and CMOTHY, as determined by Rietveld analysis.

Sample		CMO	CMOHY	CMOTY	CMOHTY
Peak Shape Function: **Pseudo-Voigt,**			***Phase Structure:*** **Tetragonal [$I4_1/a$ (88)]**		
Lattice Parameters of	**a=b (Å)**	(5.226±4) x10^{-5}	(5.223±1.5) x10^{-4}	(5.224±4) x10^{-5}	(5.227±3) x10^{-5}
	c (Å)	(11.441±1.5) x10^{-4}	(11.410±4.5) x10^{-4}	(11.433±1.5) x10^{-4}	(11.428±1.1) x10^{-4}
	α = β = γ=90				
	Volume (Å^3)	(312.580±5) x10^{-3}	(311.301±1.8) x10^{-2}	(312.086±5) x10^{-3}	(312.355±4) x10^{-3}
	Density (g/cm^3)	4.250	5.083	5.091	5.126
Residuals Refinement	**R_p (%)**	4.12	8.24	6.86	3.80
	R_{wp} (%)	5.75	11.4	9.16	5.35
	R_{exp} (%)	2.25	4.90	2.21	2.22
	χ^2 (%)	6.56	5.41	6.23	5.80

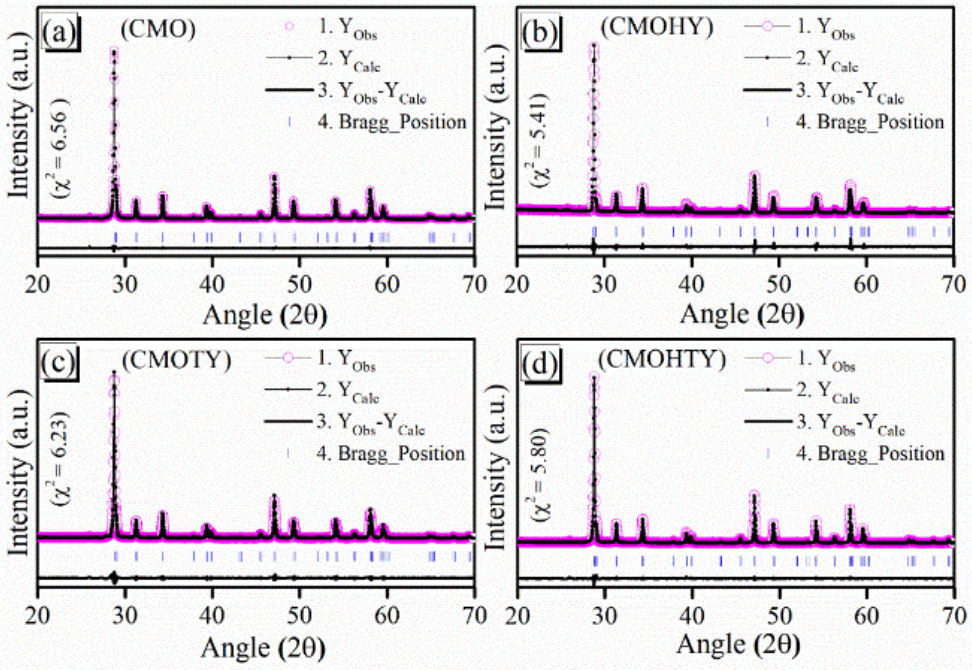

Figure 5.2 Rietveld refinement of XRD plots of CMO, CMOHY, CMOTY, and CMOHTY phosphors.

Morphological assessments of developed phosphor samples were performed by SEM image analysis taken at various resolutions. The SEM images of CMO phosphors reveal mostly agglomerated, distorted spherical forms with an average particle size of approximately 185 nm, as seen in Fig. 5.3(a) [152]. Particle distribution plots are provided in the insets of each SEM image. Doping of Ho^{3+}/Yb^{3+} ions in the CMO lattice results in a partially refined spherical morphology with an average particle dimension of around 400 nm, whereas the incorporation of Tm^{3+}/Yb^{3+} ions yields almost spherical morphology with an average particle size of around 800 nm, as seen in Fig. 5.3(b-c). Furthermore, the tri-doped ($Ho^{3+}/Tm^{3+}/Yb^{3+}$) CMO phosphor intriguingly acquired an oval morphology with varied dimensions, averaging 1500 nm in length, as seen in Fig. 5.3(d). Dopants significantly affect the growth kinetics of particles, resulting in morphological changes that enhance the propensity for agglomeration. Specifically, the heteromorphic substitution of Ca^{2+} ions with rare earth elements such as Ho^{3+}, Tm^{3+}, or Yb^{3+} introduces interstitial oxygen vacancies. These vacancies can facilitate the agglomeration of particles, resulting in refined structures that exhibit spherical or oval shape structures. It is worth noting that an increase in crystallite and particle size may contribute to improved optical properties. The elemental analysis of phosphor samples using EDAX spectra concurrently reflects the incorporation of different lanthanide ions (shown in bottom of each SEM images), which distinctly indicates the presence of Ca, Mo, and O (host constituents), together with traces of the doped elements Ho, Tm, and Yb.

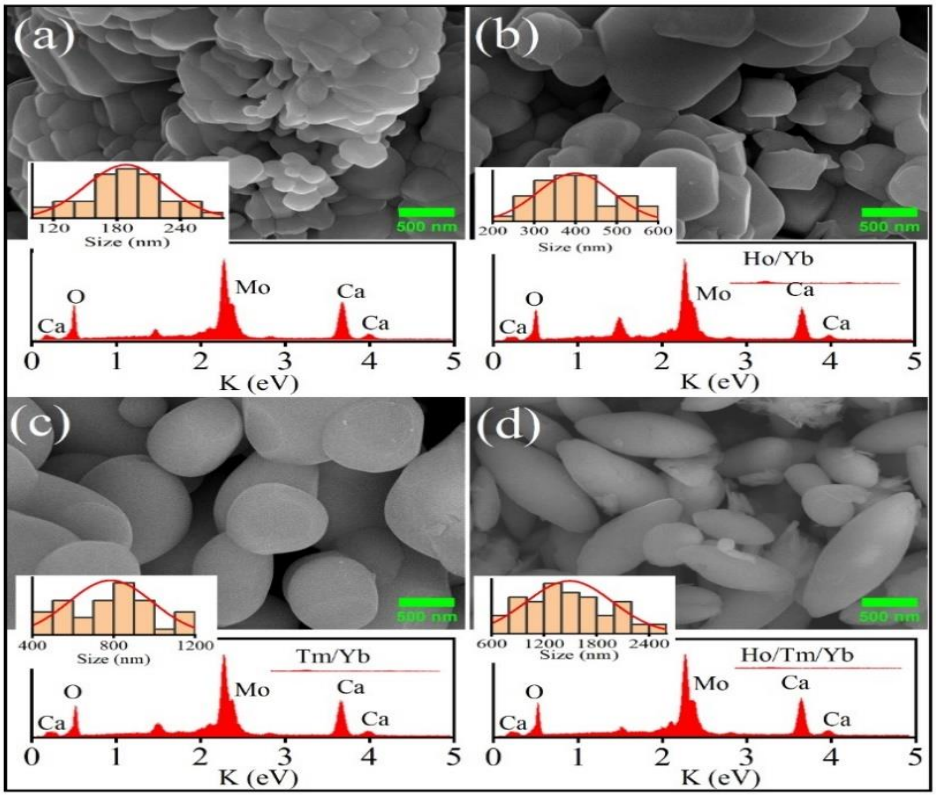

Figure 5.3 SEM images of (a) CMO, (b) CMOHY, (c) CMOTY, and (d) CMOHTY phosphors sample along with EDAX analysis (in bottom of respective micrograph) with particle size distribution plots (as inset).

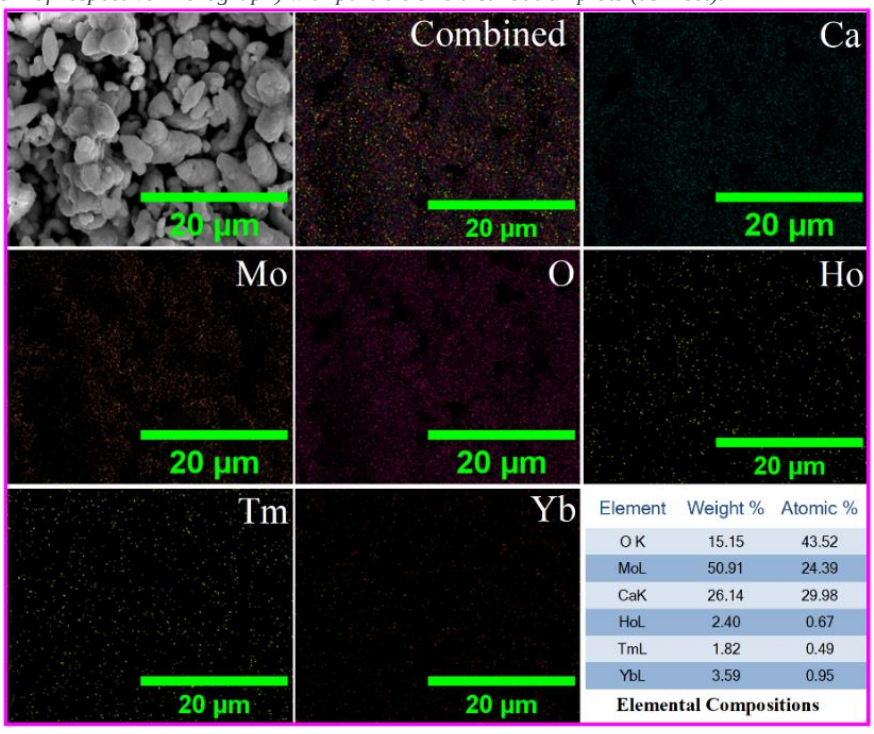

Figure 5.4 Elemental mapping of a selected region of the CMOHTY phosphor sample.

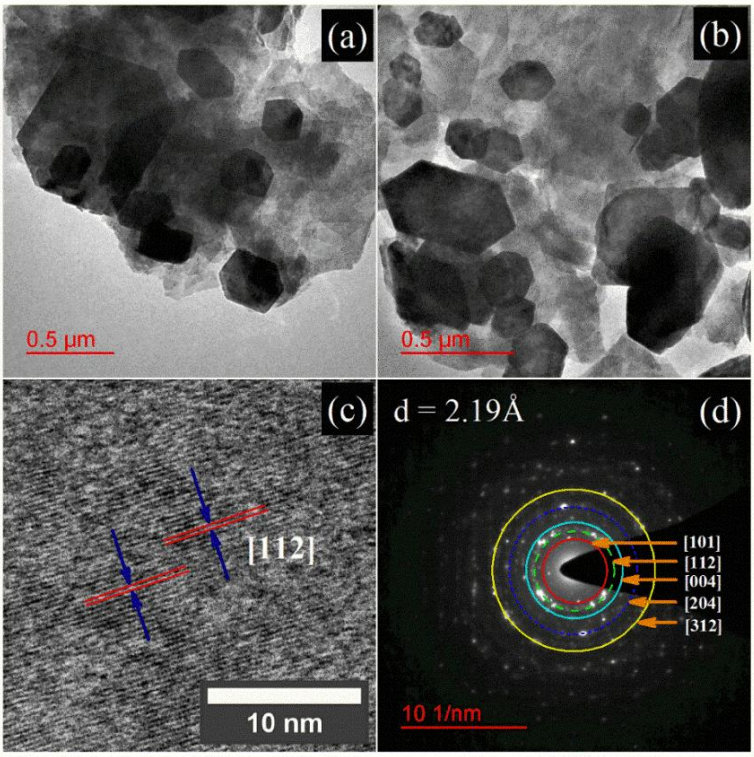

Figure 5.5 (a-b) TEM images of optimized CMOHTY phosphors at varying resolutions, (c) Interference fringes of the [112] lattice plane, (d) SAED pattern.

Selected area EDS mapping (elemental mapping) of CMOHTY phosphors further corroborates the homogeneous elemental distribution over the sample's surface, as seen in Fig. 5.4. Weight percentage of each element in CMOHTY is also listed in the Fig. 5.4. TEM images of CMOHTY phosphors calcined at 750°C, depicted in Fig. 5.5(a-b), reveal the actual rutile shape of the particles throughout various distribution ranges. The interference fringe pattern caused by a fundamental lattice plane (112) having an interplanar spacing (d-value) of 2.19 Å is seen in Fig. 5.5(c). Furthermore, the SAED patterns exhibited distinct dotted ring formations, indicating that the developed phosphors were mainly polycrystalline as displayed in Fig. 5.5(d) [154]. The prominent diffuse ring in the pattern is overlaid on a singular sharp point, with the brightest diffraction ring matching to the (112) diffraction plane of $CaMoO_4$ lattice.

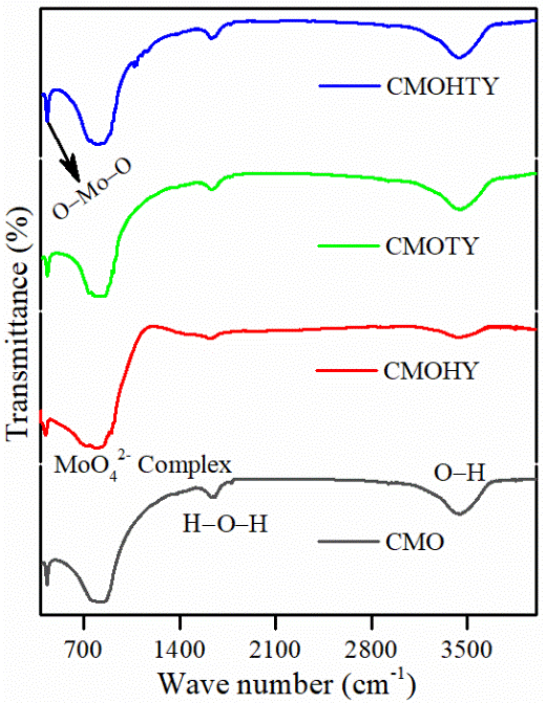

*Figure 5.6 FTIR spectra (transmittance mode) of **(a)** CMO, **(b)** CMOHY, **(c)** CMOTY and **(d)** CMOHTY phosphors sintered at 750 °C.*

5.3.2 Vibrational mode analysis

Developed samples were also examined by Fourier transform infrared (FTIR) spectroscopy to evaluate the existing vibrational modes in the phosphor samples. Fig. 5.6 displays the FTIR spectra of CMO, CMOHY, CMOTY, and CMOTHY recorded in transmittance mode within the range of 400-4000 cm^{-1}. The prominent vibrational band in pristine CMO as well as doped CMO samples display the bands occurring at around 428, 812, 1629 and 3459 cm^{-1} [8]. The most significant vibrational bands in pure CMO and doped samples occur at around 428 cm^{-1} and 812 cm^{-1}, indicating the formation of a $CaMoO_4$ lattice [9]. The band appearing at 428 cm^{-1} is attributed to bending vibration of Mo-O bond present in the MoO_4^{2-} tetrahedron, whereas the strong depth band at 812 cm^{-1} is arising due to anti-symmetric vibration of O-Mo-O present in the MoO_4^{2-} complex [155]. This suggests tetrahedral coordination of molybdenum atoms, resulting in a four-sided pyramid containing

oxygen atoms at its vertices. In addition, the bands at 1629 cm^{-1} (H-O-H bending) and 3459 cm^{-1} (O-H stretching) are attributed to absorbed H_2O molecules to the lattice, demonstrating a slightly hygroscopic nature of the sample [156].

5.3.3 UV-Visible-NIR absorption and bandgap analysis

The UV-Vis absorption spectra in reflectance mode were employed to figure out the host absorption and the dopant optical characteristics in pristine CMO and three other doped samples, i.e., CMOHY, CMOTY and CMOHTY. Fig. 5.7(a) depicts the UV-Vis spectra of the CMO host, representing the band absorbance between 200-400 nm due to the optical absorption of the molybdate tetrahedron (MoO_4^{2-}) group [9]. Additionally, the modest dopant concentration of Ln^{3+} (Ho^{3+}/Tm^{3+}/Yb^{3+}) still appears with reasonable intensity, verifying their presence and exhibiting considerable excitation bands. The absorbance band appeared in the visible region at 454 nm, 541 nm and 644 nm, corresponding to $^5I_8 \rightarrow {}^5G_6$, $^5I_8 \rightarrow {}^5F_4$ ($^5S_2$) and $^5I_8 \rightarrow {}^5F_5$ intrinsic electronic transition, respectively, attributed to intrinsic Ho^{3+} ions absorption. While the absorbance bands situated at 688 nm and 795 nm, which are related to $^1G_4 \rightarrow {}^3F_4$ and $^3H_6 \rightarrow {}^3H_4$ electronic transition, correspond to intrinsic Tm^{3+} ions absorption. Furthermore, the Yb^{3+} ions absorption bands at 976 nm ($^2F_{7/2} \rightarrow {}^2F_{5/2}$) were used to establish the UC spectra.

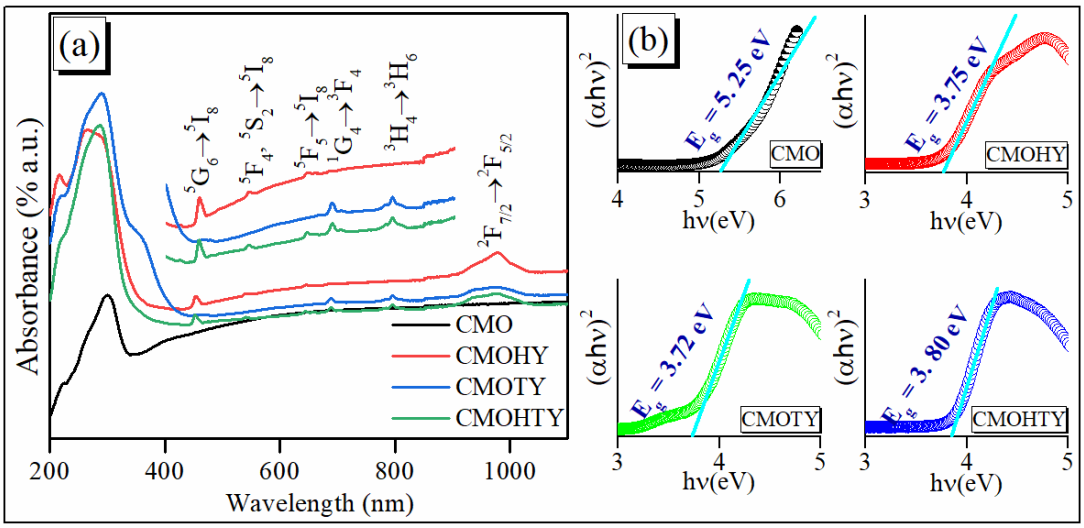

Figure 5.7 ***(a)*** *UV-Vis absorption spectra of CMO, CMOHY, CMOTY, and CMOHTY phosphor materials.* ***(b)*** *Tauc plot illustrating the bandgap of the same materials.*

In pristine CMO, an absorption cut edge is noted near 300 nm, aligning with its bandgap, which shifts in more uv region by nearly 10 nm following doping of Ln^{3+} ions, clearly signifying a reduction in the optical bandgap. Tauc plots [$(\alpha h\nu)^2$ *vs* hν], seen in Fig. 5.7(b), are employed to ascertain the bandgap (E_g) of the phosphors sample. The pristine CMO sample demonstrates an obvious band gap of approximately 5.25 eV, while a significant decrease in the band gap is noted upon Ln^{3+} doping. The optical bandgap of the CMOHY, CMOTY, and CMOHTY phosphor samples is around 3.72 eV, 3.70 eV, and 3.80 eV, respectively. The discrepancies observed in the optical bandgap (E_g) values between doped and undoped phosphors can be attributed to the introduction of localised energy states within the bandgap, the ionic size of the dopants, and the charge compensation mechanisms that enable the emergence of vacancies, defects or disorder, particularly as a result of the substitution of Ca^{2+} by Ln^{3+} ions [157]. The defects or vacancies resulting from Ln^{3+} (Ho^{3+}, Tm^{3+}, and Yb^{3+}) doping establish a significant potential gradient within the host matrix. This gradient leads to the quantum mechanical penetration of localised states into the forbidden

band gap. These states can also serve as charge carrier recombination sites, thereby reducing the energy difference between the conduction and valence bands.

5.3.4 Infrared to visible Upconversion emission analysis

The photon up-conversion process in Ho^{3+} ions is widely recognized for its emission in the green and red regions of the EM spectrum; nevertheless, its emission efficiency is primarily influenced by the host's crystallographic asymmetry, morphology, particle size, and also foreign dopants, among other factors. Moreover, the dominance of the particular band's emission is attributed to the phonon frequency. Doping Ho^{3+}/Yb^{3+} (in mol%) in $CaMoO_4$ yields dazzling green emitting bands at 545 nm, as well as relatively small red (655 nm) and NIR emission (755 nm) bands under 980 nm excitation, which spans the mid-visible region as shown in Fig. 5.8. Intense green emission of Ho^{3+} ions is attributed to the $^5S_2/^5F_4 \rightarrow ^5I_8$. In contrast, the red and NIR emission is due to the $^5F_5 \rightarrow ^5I_8$ and $^5S_2/^5F_4 \rightarrow ^5I_7$ electronic transitions, respectively [158]. Through experimental exploration, the ideal concentration of Ho^{3+} ions for optimal upconversion (UC) performance is determined to be approximately 0.3 mol%, with Yb^{3+} ions held constant at 10 mol%. This configuration is designated as CMOHY phosphors. However, increasing the Ho^{3+} concentration beyond this point leads to concentration quenching, resulting in diminished emission when subjected to near-infrared (NIR) excitation.

Meanwhile, precisely Tm^{3+}/Yb^{3+} doping, referred to as CMOTY, emits in the blue (473 nm) and NIR (795 nm) regions of the EM spectrum, ascribed to $^1G_4 \rightarrow ^3H_6$ and $^1F_2 \rightarrow ^3H_6$ ($^3H_4 \rightarrow ^3H_6$) electronic transitions, respectively [159]. Numerous studies indicate that the optimal doping concentration for Tm^{3+} ions typically ranges from 0.5 to 1 mol% [160]. In this context, the ideal concentration of Tm^{3+} in $CaMoO_4$ has been identified as 0.7 mol%, with

Yb^{3+} ions consistently held at 10 mol%. The goal is to harness temperature-sensing properties derived from the non-thermally coupled levels (NTCLs) of doped Ln^{3+} ions. Doping of Ho^{3+}/Tm^{3+} encompasses multiple emitting bands covering the visible range, allowing for selecting a distinct set of emitting bands. Therefore, an integrated Ho^{3+}/Tm^{3+} doped phosphor with two optically active centres is employed to harvest the emission characteristics, referred to as CMOHTY. Now, we have four emitting bands corresponding to Ho^{3+} and Tm^{3+} ions emission, showing the temperature-dependent behaviour, which is further employed to study the temperature sensing application.

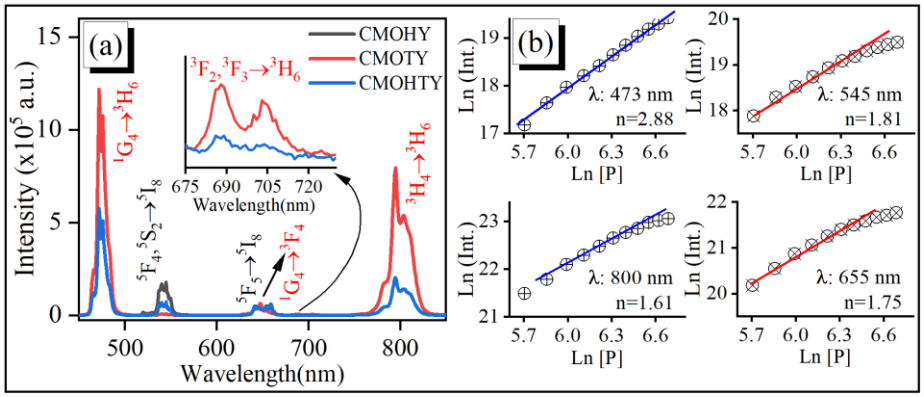

Figure 5.8 ***(a)*** *Upconversion spectra of the optimized CMOHY, CMOTY, and CMOHTY phosphor materials.* ***(b)*** *Ln-Ln plot corresponding to different emitting bands under 980 nm excitation.*

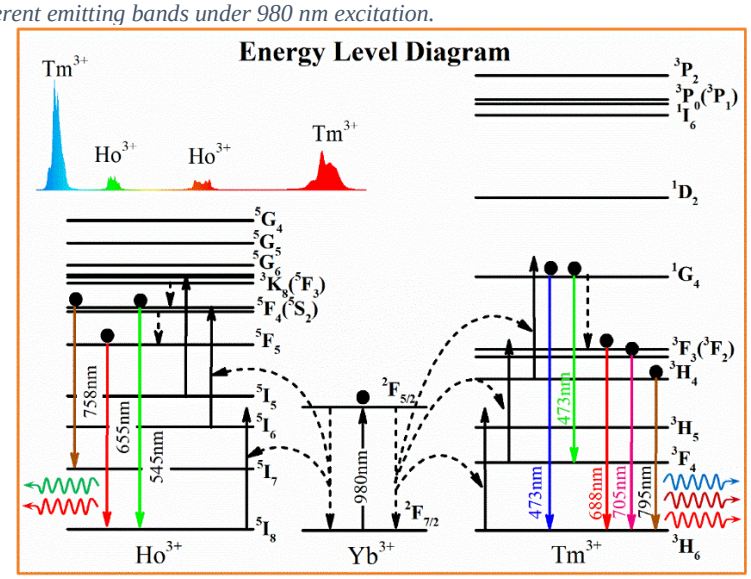

Figure 5.9 Schematic energy level diagram of $Ho^{3+}/Tm^{3+}/Yb^{3+}$ ions with potential UC mechanisms.

An analysis of power-dependent UC emission intensity has been performed to ascertain the number of photons engaged in the UC process in the CMOHTY phosphor sample. Power-dependent UC is determined using the equation (I_{up} α P^n), where I_{up} is integrated intensity, P is excitation power, and n is the number of photons needed to reach the emission level [8]. It shows that almost two NIR photons are involved in getting green and red UC emissions [~1.81 (green) and ~1.71 (red)] from Ho^{3+} ions, which is reasonable for the UC emission mechanism. For Tm^{3+} ion, UC emission exhibited almost 3 photons for blue emission and 1.5 photons for red emission. The reasonable UC emission mechanism for both Ho^{3+} and Tm^{3+} ions can be seen in the energy level diagram [Fig. 5.9].

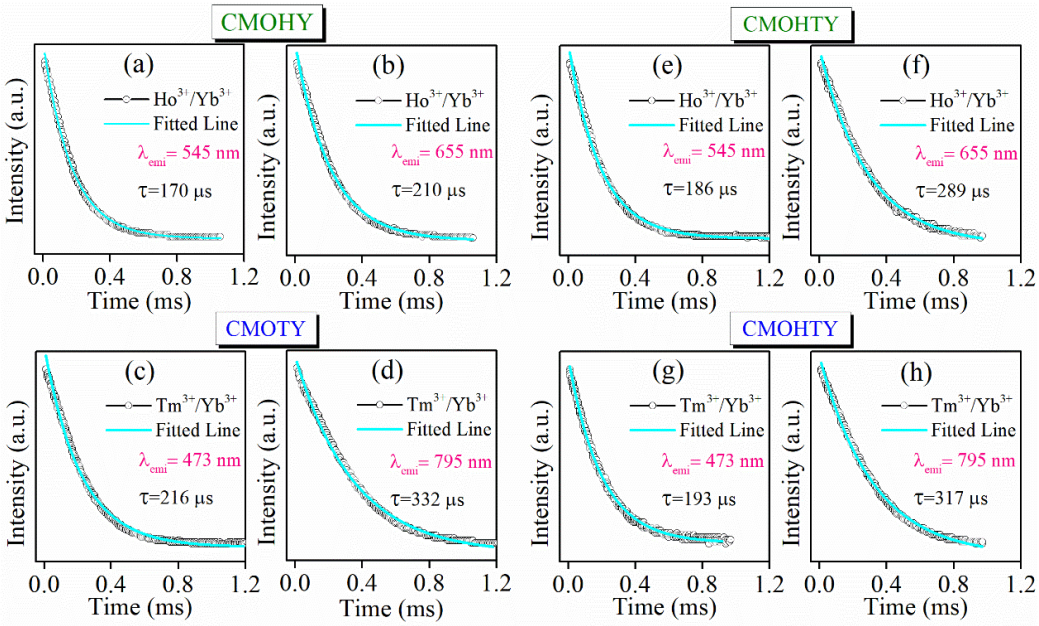

Figure 5.10 Decay time analysis of different emitting bands i.e., (a-b) CMOHY (Ho^{3+} λ_{emi}=545 nm, 655 nm) and (c-d) CMOTY (λ_{emi}=473 nm, 795 nm), (e-f) CMOHTY (λ_{emi}=545 nm, 655 nm) and (g-h) (λ_{emi}=473 nm, 795 nm) under 980 nm excitation.

Investigating the decay times across different emission bands of Ho^{3+} and Tm^{3+} ions under 980 nm excitation reveals single exponential function fitting of decay profile. This suggests a singular pathway for population build up in the excited states of both ions. Lifetime of each state, is determined by fitting the decay curve to a single exponential function, expressed as

$I=I_o \exp(-t/\tau)$, where τ denotes the lifetime of the state. Fig. 5.10 displays the fitted decay curves for the key emitting states associated with Ho^{3+} and Tm^{3+} ions in the phosphor samples CMOHY, CMOTY, and CMOHTY under 980 nm excitation, along with a detailed description. Notably, lifetimes of Ho^{3+}'s green ($^5F_4/^5S_2$) and red ($^5F_5$) emission states in CMOHTY, is slightly enhanced in CMOHTY compared to those in CMOHY. In contrast, the emitting states of Tm^{3+} at 473 nm ($^1G_4 \rightarrow {}^3H_6$) and 795 nm ($^3H_4 \rightarrow {}^3H_6$) show a significant reduction in lifetime in CMOHTY compared to CMOTY. This notable decrease in Tm^{3+}'s lifetime is attributed to energy transfer to Ho^{3+}, providing strong evidence of the interaction between Tm^{3+} and Ho^{3+} ions, as discussed Liu *et al* [161]. Additionally, Huang *et al* reported that the energy transfer is likely due to an enhanced rate of two cross-relaxation processes between Tm^{3+} and Ho^{3+} ions at elevated Tm^{3+} doping concentrations, which accelerates the radiative relaxation processes of Ho^{3+} ions involving $^5S_2/^5I_8$ and $^5F_5/^5I_8$ transitions [162].

5.4 Multifunctional behaviour of CMOHTY phosphor

5.4.1 Temperature Sensing application

An assessment of the temperature sensing potential of the developed phosphor materials, i.e., $CaMoO_4:Ho^{3+}/Tm^{3+}/Yb^{3+}$ (CMOTHY), is carried out by tracking the fluorescence intensity emitted by doped Ln^{3+} ions with a variation of external temperature. For this purpose, the fluorescence intensity ratio (FIR) of different emission bands that respond well to temperature is calculated. There exists a varying degree of temperature-dependent response in the emission bands of Tm^{3+} (473 nm, 795 nm) and Ho^{3+} (545 nm, 655 nm), with an apparent decrease in emission intensity as temperature increases as shown in Fig. 5.11. In general, the chance of non-radiative transition is dominated with the rise of temperature, hence the emission intensity reduces, which is usually referred as temperature quenching phenomenon

[163]. In some instances, the emission intensity initially exhibits an upward trend in low-temperature constraints; whereas, as the temperature nears a critical threshold, non-radiative relaxation begins to predominate with an additional increase in temperature, attributable to the relative competition between non-radiative relaxation and temperature quenching effects. Furthermore, the phenomenon of thermal quenching is explicitly correlated with the phonon frequency of the host matrix. Indeed, a higher phonon frequency would lead to a readily decreased emission intensity, ascribed as multi-phonon non-radiative relaxation [164].

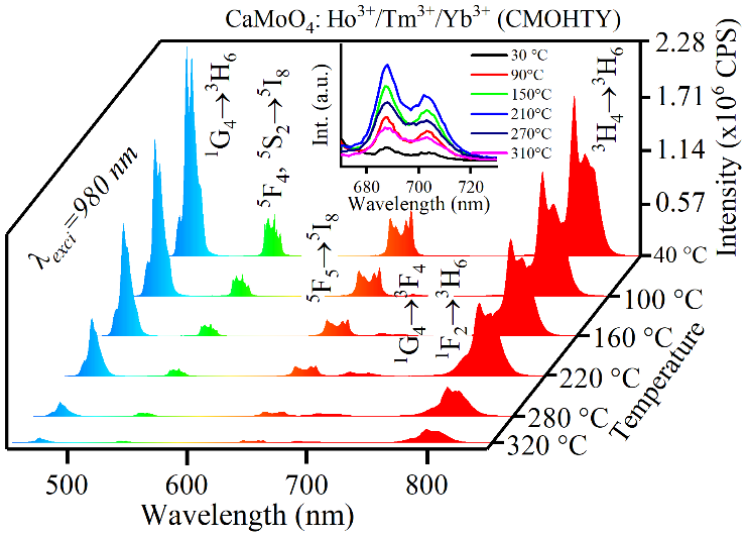

Figure 5.11 Temperature-dependent UC emission of CMOHTY phosphors under 980 nm excitation.

Generally, temperature sensing based on the FIR technique involves the thermally coupled levels (TCLs) of particular Ln^{3+} ions, in which the phonon-assisted population shift takes place with the temperature rise. Interestingly, two thermally coupled levels, $^1G_{4(1,2)}$ and $^3F_{2,3}$/ $^3H_4$, are commonly found in Tm^{3+} ions. Among them, the energy level $^1G_{4(1)}$ appears with remarkable intensity, while $^1G_{4(2)}$ does not show emission even with the increase in temperature [163]. Apart from that the noteworthy feature of TCLs, namely $^3F_{2,\,3,}$ and $^3H_4$, exhibit a thermally dependent emission pattern as the temperature increases up to 480 K. Subsequently, the temperature quenching effect becomes more prominent causing the

reduction of intensity, as seen in Fig. 5.11. Implementation of TCLs for temperature sensing using the FIR technique is regulated by Maxwell's Boltzmann relation and represented as follows[8].

$$FIR = \frac{I_{20}}{I_{10}} = B \exp\left(-\frac{\Delta E}{kT}\right) \quad \ldots (5.3)$$

The value of absolute temperature can be calculated as follows

$$T = \frac{\Delta E}{k} \frac{1}{\ln\left(\frac{B}{FIR}\right)} \quad \ldots (5.4)$$

The parameters I_{20} and I_{10} represent the emission levels of thermally connected upper and lower excited states, respectively, with an energy gap ΔE. B represents an arbitrary constant, k signifies the Boltzmann constant, and T denotes the absolute temperature. The related parameter signifying the performance of the materials over a specified temperature range is usually divided into absolute sensitivity (S_a) and relative sensitivity (S_r) [165].

$$S_a = \frac{\partial FIR}{\partial T} = FIR \frac{\Delta E}{kT^2} \quad \ldots (5.5)$$

$$S_r = \frac{1}{FIR} \frac{\partial FIR}{\partial T} = \frac{\Delta E}{kT^2} \quad \ldots (5.6)$$

Where S_a is defined as the FIR variation with respect to temperature per kelvin (K^{-1}), mainly employed to compare the sensitivity of similar types of materials. Whereas the S_r is employed to quantify the percentage change of the FIR with respect to its own value for a temperature variation per Kelvin (K^{-1}) and is more general to compare across the different types of materials.

In the context of this phosphor material, the TCLs emission is relatively insignificant, while the emission commencing from non-thermally coupled levels (NTCLs) of Tm^{3+}/Ho^{3+}

encompasses robust optical characteristics and demonstrates a remarkable temperature-dependent response across several emission bands [163]. For the different selected pair of NTCLs emission bands, namely I_{795}/I_{473}, I_{688}/I_{473}, I_{688}/I_{655}, and I_{688}/I_{795}, the traditional NTCLs-based FIR technique does not hold well, nevertheless, it is possible to establish the correlation between the FIR and the absolute temperature (T), which can be obtained by employing a plausible approximation based on the following equation:

$$FIR = A_2 + \frac{A_2 - A_1}{1 + exp\left(\frac{T - T_0}{Slope\ at\ T_0}\right)} \quad \ldots (5.7)$$

The function in discussion is typically known as the Boltzmann sigmoidal function. It represents exponential growth with sinusoidal characteristics, which is entirely compatible with the shape of the NTCLs FIR plots. Where A_1 and A_2 are the initial and final values of the plot and the T_0 ($=\frac{A_1+A_2}{2}$) is defined as the mid value of the plot. The fitting result in Fig. 5.12 exhibits an excellent correlation with the experimental data. It is interesting to understand the process of FIR variation with temperature for the different pairs of NTCLs. In this particular case, the intensities of Tm^{3+} bands are comparatively higher than that of Ho^{3+} bands. The existence of thermally stimulated bands of Tm^{3+} ions, often known as thermionic emission, renders them advantageous for tracking temperatures. Close observation of all fittings initially shows slight variation with temperatures up to 400 K. At the same time, the FIR ratio significantly turns to a more significant value above this temperature, probably due to multi-phonon non-radiative relaxation not much prominent at this stage [166]. Above this, the emission bands in the high energy side are effectively encountered with thermal de-excitation, along with an increase in thermionic emission situated at 688 nm. Subsequently,

the comparison of sensitivity is calculated by estimating the sensitivity parameter S_a and S_r using the following equation[167].

$$S_a = \left| \frac{\partial FIR}{\partial T} \right| \text{ and } S_r = \left| \frac{1}{FIR} \frac{\partial FIR}{\partial T} \right| \quad \ldots (5.8)$$

The relevance of S_a and S_r, are already being discussed earlier. Fig. 5.12 exhibits the temperature sensitivity of different NTCLs groups, namely I_{795}/I_{473}, I_{688}/I_{473}, I_{688}/I_{655}, and I_{688}/I_{795}. A list of the absolute and relative sensitivity of different NTCLs groups is tabulated in Table 5.2. The highest absolute sensitivity value (S_a) was observed for the I_{795}/I_{473} at 500 K, which is 69.86×10^{-2} K^{-1}. In contrast, the values of S_a for the other NTCLs were comparatively more petite, with values of 0.614×10^{-2} K^{-1} at 455 K, 8.42×10^{-2} K^{-1} at 502 K, and 0.076×10^{-2} at 536 K for the I_{688}/I_{655}, I_{688}/I_{473}, and I_{688}/I_{795} respectively. In addition, the S_r value increases with temperature. It reaches its maximum values of 1.65% K^{-1} and 3.01% K^{-1} for the FIR ratio I_{795}/I_{473} and I_{688}/I_{473} at about 445 K and 435 K, respectively, subsequently exhibiting a declining tendency with temperature decrease. Meanwhile, the highest S_r values for I_{688}/I_{655} and I_{688}/I_{795} were observed at 303 K, corresponding to 18.57% K^{-1} and 2.87% K^{-1}, respectively.

Table 5.2 details the temperature sensitivity of phosphor materials based on the NTCLs of Ho^{3+}/Tm^{3+}. Notably, the $CaMoO_4$: $Ho^{3+}/Tm^{3+}/Yb^{3+}$ sample exhibits the highest Sa value for the I_{795}/I_{473} ratio (69.8% K^{-1}) at 500 K, while the S_r value is most prominent for the I_{688}/I_{655} ratio (18.57% K^{-1}) at 303 K, with the rest ratios ending up below those values. The study concludes that CMOHTY ($Ca_{0.89}Ho_{0.003}Tm_{0.007}Yb_{0.1}MoO_4$) phosphors exhibit robust temperature sensing capabilities based on non-thermally coupled levels (NTCLs), with temperature-dependent solid responses and high sensitivity across multiple emission bands.

Notably, this work reports for the first time the NTCLs-based temperature sensing in the $CaMoO_4$ host, along with the novel application of a Boltzmann sigmoidal fitting equation to model the FIR vs. temperature behaviour of NTCLs.

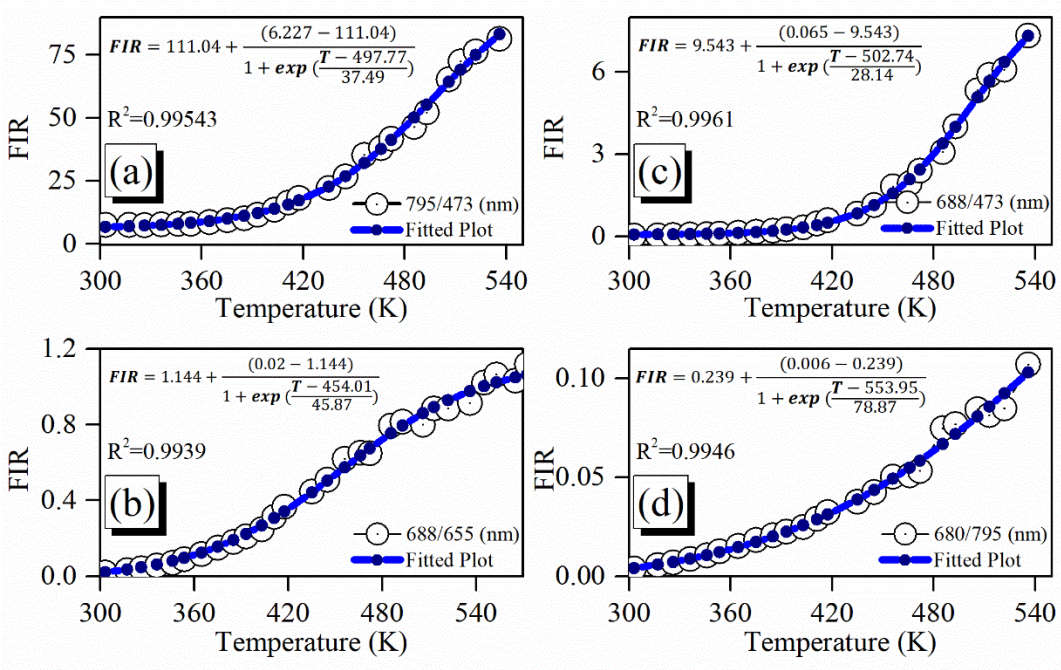

Figure 5.12 FIR vs Temperature plots fitted with a Boltzmann sigmoidal function of different sets of NTCLs: (a) I_{795}/I_{473}, (b) I_{688}/I_{473}, (c) I_{688}/I_{655}, and (d) I_{688}/I_{795} of CMOHTY phosphors sample.

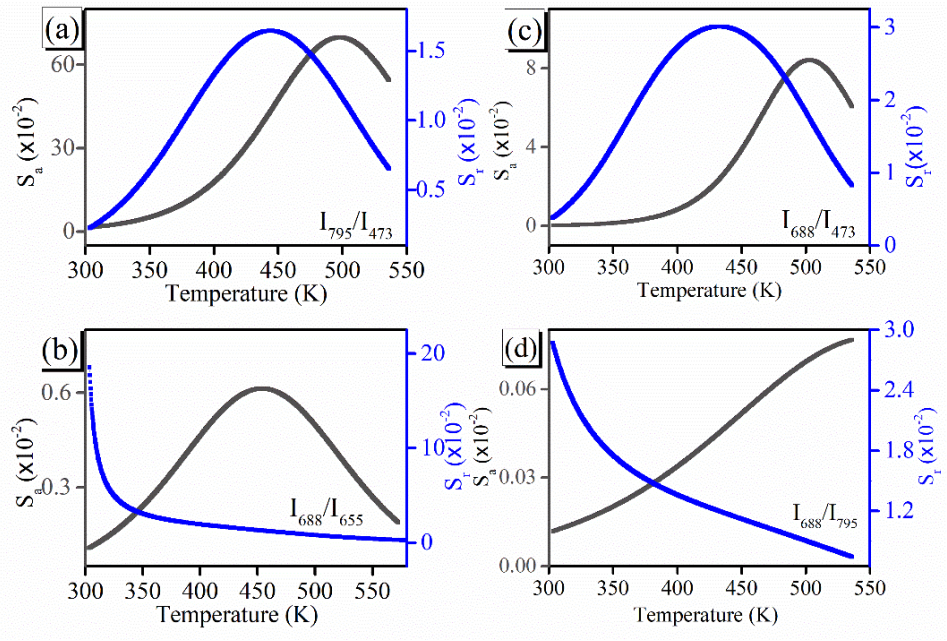

Figure 5.13 Relative (S_r) and absolute sensitivity (S_a) plots for different sets of NTCLs, fitted to Boltzmann sigmoidal function.

Table 5.2 Comparison of temperature sensing characteristics based on FIR technique using NTCLs of Ho^{3+}/Tm^{3+} in various hosts with the involved transition.

Host: $Ho^{3+}/Tm^{3+}/Yb^{3+}$	I_1/I_2	Transitions	ΔE [cm^{-1}]	Max S_a [% K^{-1}]	Max S_r [% K^{-1}]	Ref.
$NaYF_4$	I_{696}/I_{541}	$^3F_3 \rightarrow {}^3H_6$ (Tm)/ $^5F4 \rightarrow {}^5I_8$ (Ho)	3980	0.059 [495K]	0.711 [320 K]	[163]
	I_{696}/I_{474}	$^3F_3 \rightarrow {}^3H_6$ (Tm)/$^1G_4 \rightarrow {}^3H_6$ (Tm)	6607	0.87 [495 K]	0.944 [445 K]	
	I_{696}/I_{522}	$^3F_3 \rightarrow {}^3H_6$ (Tm)/$^5F_3 \rightarrow {}^5I_8$ (Ho)	732	1.26 [495 K]	1.796 [345 K]	
	I_{696}/I_{644}	$^3F_3 \rightarrow {}^3H_6$ (Tm)/$^5F_5 \rightarrow {}^5I_8$ (Ho)	1956	0.057 [495 K]	0.955 [345 K]	
$BaIn_2O_4$	I_{795}/I_{480}	$^3F_4 \rightarrow {}^3H_6$ (Tm)/$^1G_4 \rightarrow {}^3H_6$ (Tm)	8563	25.45 [473 K]	1.48 [456 K]	[80]
	I_{795}/I_{550}	$^3H_4 \rightarrow {}^3H_6$ (Tm)/$^5F_4 \rightarrow {}^5I_8$ (Ho)	5603	1.83 [473 K]	0.48 [353 K]	
	I_{550}/I_{666}	$^5F_4 \rightarrow {}^5I_8$(Ho)/$^5F_5 \rightarrow {}^5I_8$ (Ho)	3167	3.32 [353 K]	0.44 [353 K]	
	I_{480}/I_{666}	$^1G_4 \rightarrow {}^3H_6$ (Tm)/$^5F_5 \rightarrow {}^5I_8$ (Ho)	5818	4.05 [353 K]	1.95 [473 K]	
	I_{550}/I_{480}	$^5F_{54} \rightarrow {}^5I_8$ (Ho)/$^1G_4 \rightarrow {}^3H_6$ (Tm)	2651	4.89 [473 K]	1.19 [473 K]	
$Ba_3Y_4O_9$	I_{803}/I_{482}	$^3H_4 \rightarrow {}^3H_6$ (Tm)/$^1G_4 \rightarrow {}^3H_6$ (Tm)	8294	5.52 [575 K]	0.34 [575 K]	[168]
Y_2O_3	I_{477}/I_{488}	$^1G_4 \rightarrow {}^3H_6$ (Tm)/$^5F_3 \rightarrow {}^5I_8$ (Ho)	472	0.696 [303 K]	0.34 [303 K]	[169]
$NaLa(MoO_4)_2$	I_{695}/I_{545}	$^3F_3 \rightarrow {}^3H_6$ (Tm)//$^5F_{54} \rightarrow {}^5I_8$ (Ho)	3960	2.848 [308 K]	1.63 [308 K]	[170]
$Gd_2(WO_3)_2$	I_{700}/I_{540}	$^3F_3 \rightarrow {}^3H_6$ (Tm)//$^5F_{54} \rightarrow {}^5I_8$ (Ho)	4233	2.614 [595 K]	--	[171]
$KLu(WO_3)_2$	I_{696}/I_{545}	$^3F_3 \rightarrow {}^3H_6$ (Tm)/$^5F4 \rightarrow {}^5I_8$ (Ho)	3980	--	0.60 [295 K]	[172]
$CaMoO_4$	I_{795}/I_{473}	$^3H_4 \rightarrow {}^3H_6$ (Tm)/$^1G_4 \rightarrow {}^3H_6$ (Tm)	8563	69.86 [500 K]	1.65 [445 K]	*Present Work
	I_{688}/I_{473}	$^1G_4 \rightarrow {}^3F_4$ (Tm)/$^1G_4 \rightarrow {}^3H_6$ (Tm)	6607	8.42 [502 K]	3.01 [435 K]	
	I_{688}/I_{655}	$^1G_4 \rightarrow {}^3F_4$ (Tm)/$^5F_5 \rightarrow {}^5I_8$ (Ho)	732	0.614 [455 K]	18.57 [303 K]	
	I_{688}/I_{795}	$^1G_4 \rightarrow {}^3F_4$ (Tm)/$^3H_4 \rightarrow {}^3H_6$ (Tm)	1956	0.20 [572 K]	131 [572 K]	

5.4.2 Latent Fingerprints (LFPs)

As previously stated, the versatile optical properties of $Ho^{3+}/Tm^{3+}/Yb^{3+}$ doped $CaMoO_4$ phosphor materials result in emission throughout the visible spectrum, with prominent emission for Tm^{3+} ions and relatively weak emission for Ho^{3+} ions. Furthermore, the individual emission can be easily distinguished by using a particular optical filter. Consequently, integrating fluorescent powder to visualise latent fingerprints (LFPs) would be more intriguing due to the inherent exhibition of different colours in materials under NIR excitation. Generally, the most appropriate 'powder dusting' technique for acquiring LPFs on various substrates entails a specified set of detection processes [173]. In the dusting technique, the relevance of employed powder depends on adherence to an aqueous or oily substance on the substrate, allowing for clear visibility and definition of the latent print. Furthermore, the particle size, shape, relative surface area, and surface charge would also play a significant role. In conventional methods for detecting latent prints, UV lamps are commonly employed

with various powders such as white or grey powder, fluorescent powder, magnetic powder, and black powder. These LFP powders are often composed of a specific pigment for good visibility, offering high contrast and resolution against background surfaces that clanged with an appropriate resilient carrier, as reported in multiple literature. The choice of powder depends on the surface type (substrate), such as porous, nonporous, coloured, and multitextured surfaces, as well as prevailing circumstances [174].

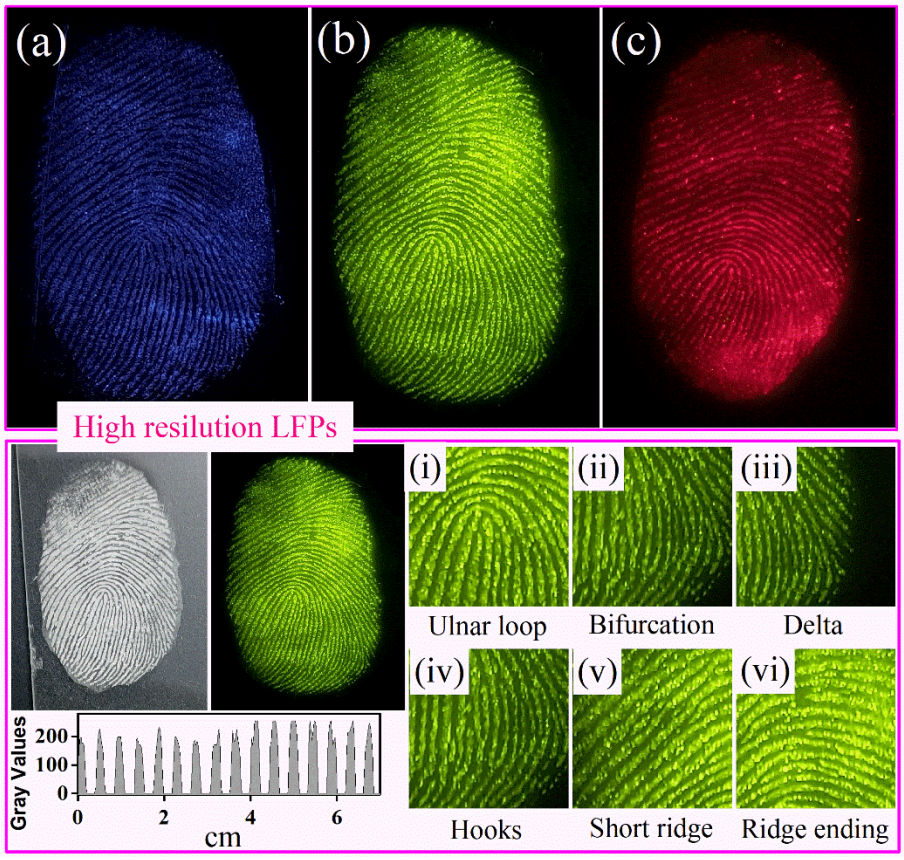

Figure 5.14 (a-c) Coloured LFP images were acquired using CMOHTY powder phosphors dusted over a glass plate substrate under 980 nm excitation, utilizing filters and high-resolution images of the green LFPs with various minutiae.

Herein, the $CaMoO_4:Ho^{3+}/Tm^{3+}/Yb^{3+}$ phosphor materials employed for latent fingerprinting through the 'dusting approach' have the advantage of capturing simultaneous coloured pictures due to their moisture affinity and propensity to cling to friction ridge skin residue without staining the substrate [175]. Intense blue, green, and red colours when

subjected to near-infrared (NIR) excitation indicate the exceptional visibility of LFPs, which facilitates high contrast and adequate definition of prints as depicted, as shown in Fig. 5.14. Generally, the distribution of ridge patterns, minutiae characteristics, ridge width and sweat pores are the main features employed to identify individual fingerprints, often categories in a hierarchical sequence. Fig. 5.14 shows a high-resolution coloured LFPs image of a volunteer acquired with consent with detailed information. The first recognition step involves identifying basic patterns such as loops, whorls, arches, etc [176]. An ulnar loop pattern is found in the present case, as depicted in Fig. 5.14 (i). The uniqueness of LFPs by examining the details of different numbers of minutiae and their related positions, categorized under second recognition steps, specifically including (ii) Bifurcation, (iii) Delta, (iv) Hooks, (v) short ridge, (vi) Ridge ending; demonstrated in high-resolution LFPs [Fig. 5.14]. Ultimately, the ridge structure and its distinct properties, including the distribution of sweet pores (positioned centrally or peripherally on the ridges) and the curvature of the ridges, determine the authenticity and distinctiveness of individual LFPs. The typical ridge width ranges from 180 – 320 μm, and the average ridge intensity is almost uniform. Moreover, the scars found in prints may result from accidents, occupational activities, and ageing, which substantially aid in recognizing patterns; however, this is irrelevant in this case. In recent decades, predetermined computer algorithms have entirely replaced the traditional methods of understanding and reading the LFPs. These algorithms facilitate individual identification and allow for the creation of a reliable database. The acquisition of LFPs using the 'dusting method' with this developed fluorescent powder produces a clear and detailed image with excellent contrast and resolution compared to the surrounding surfaces. This ensures precise

identification and enhances the reliability and validity of fingerprint analysis in forensic investigations[177].

5.5 Conclusion

This chapter concludes that the synthesis of Ho^{3+}/Yb^{3+}, Tm^{3+}/Yb^{3+} and $Ho^{3+}/Tm^{3+}/Yb^{3+}$ doped $CaMoO_4$ phosphors materials using hydrothermal technique followed by post-calcination at 750 °C. Phase analysis confirms establishing a tetragonal crystalline structure of $CaMoO_4$, doped with lanthanides, devoid of impurity peaks. The increase of particle size and their modification towards spherical then oval shape happens due to disparity in dopant valency as observed in SEM images. FTIR and UV-Vis investigations confirmed the establishment of a tetragonal lattice and the effective integration of dopant ions, evidenced by distinct vibrational modes and absorption bands, respectively. The strong up-conversion (UC) emission of the synthesized phosphors, together with the potential mechanism involved in the UC mechanism, is substantiated by a power-dependent UC investigation. For temperature sensing application, the different sets NTCLs emission are taken into interest, which is further fitted with Boltzmann sigmoidal function, showing up the largest absolute sensitivity for the I_{795}/I_{473} (69.86×10^{-2} K^{-1} at 500 K). Additionally, the synthesized phosphors also exhibit the excellent performance in LFPs imaging. The distinct multi-colour emissions under NIR excitation provided high contrast and clear visibility of ridge patterns, enabling detailed analysis of fingerprint pattern. Overall, the findings of this research underscore the versatility and efficacy of $CaMoO_4$-based phosphors in both temperature sensing and forensic applications.